One-pot hydrothermal synthesis of a hierarchical nanofungus-like anatase TiO$_2$ thin film for photocatalytic oxidation of bisphenol A

Jiawei Ng, Xiaoping Wang, Darren Delai Sun*

Division of Environmental and Water Resources Engineering, School of Civil and Environmental Engineering, Nanyang Technological University, Block N1, 50 Nanyang Avenue, Singapore 639798, Singapore

ARTICLE INFO

ABSTRACT

This article reports the synthesis of an anatase thin film bearing a unique, hierarchical nanofungus-like structure. The nanostructures were directly grown from a Ti substrate via a facile, one-pot hydrothermal reaction, thus rendering ease of catalyst separation, recycle and reuse. High-resolution images of field emission scanning electron microscope (FESEM) indicated presence of small titania nanoparticulates of *ca.* 20 nm on the nanoflakes, which constitute to the final overall nanofungus-like morphology. Hydrothermal duration-progressive FESEM images illustrated evolution of the nanofungus-structure and provided some evidence of the probable mechanism in obtaining the final nanostructure. The crystallographic phases and orientation of the photocatalyst were investigated by X-ray diffraction (XRD) and transmission electron microscopy (TEM). Nitrogen adsorption–desorption isotherm indicated that the as-prepared catalyst possessed a mesoporous structure and a Brunauer–Emmett–Teller (BET) surface area of 102.1 m^2/g. Greater light absorbance as shown from the UV–vis diffuse reflectance spectra, denoted enhanced light harvesting effects for UV penetration, possibly induced by inherent mesopores. Surface elemental analysis by means of X-ray photoelectron spectroscopy (XPS) and energy-dispersive X-ray spectroscopy (EDX) underlined purity of the titania sample with detected presence of only Ti and O in the sample. High resolution XPS scan of F 1s region revealed presence of fluoride ions adsorbed on the surface of TiO$_2$, which promoted etching and surface fluorination within the acidic hydrothermal environment. The photocatalyst exhibited efficient photocatalytic degradation of Bisphenol A (BPA) under UV-A irradiation, in comparison with a Degussa P25 TiO$_2$ coated film. The mechanism behind UV photocatalytic degradation of BPA over TiO$_2$ was elucidated using charge-trapping species as diagnostic tools and evidence have shown hydroxyl radicals (•OH) to be the predominant active species in associated oxidation processes.

1. Introduction

Considerable research efforts have been carried out in the controllable fabrication and characterization of titanium dioxide (TiO$_2$) in various dimensionalities and morphologies [1,2]. As an important wide bandgap semiconductor, various nanofeatures of TiO$_2$ have been explored to optimize properties and improve efficiencies. Among the wide array of nanostructures, nanowires [3,4], nanotubes [5,6], nanobelts [7,8], nanoflakes [9,10], nanospheres [11,12] and nanorods [13,14], are some of the more commonly reported architectures.

However, one of the main problems hampering engineering applications of TiO$_2$ today is the constraints of recovering spent catalyst from treated effluent [15]. This holds true especially for powdered suspension in fluidized bed systems, where nanopowdered photocatalysts can potentially become a form of secondary contamination in environmental remediation processes. In view of the practical limitations and predicament of nanopowdered photocatalysts, different strategies to immobilize nanoparticulate TiO$_2$ on solid substrates have thus been proposed [10,16,17]. However, due to the tedious preparation process and weak particulate attachment on foreign substrates, such supported photocatalysts are largely restricted to laboratory or small scale applications. Over the last decade, there has been a shift in research focus on development of porous titania thin film structures. Scientists have proposed various synthetic methods to induce direct crystal growth of TiO$_2$ nanostructures over Ti substrates, for instance, anodization [5,6], sol–gel (spin or dip coating) [18], hydrothermal [3,9,11,13,14,19,20], chemical vapor deposition [21], physical vapor thermal deposition [22], and template-based assembly using structure-directing agents [23,24], etc.

From the research bibliography of inorganic hierarchical nanostructures, it is not difficult to observe that the hydrothermal

* Corresponding author. Tel.: +65 6790 6273; fax: +65 67910676.
E-mail address: ddsun@ntu.edu.sg (D.D. Sun).

method is one of the most common techniques employed. Contrary to other methods of crystal growth, hydrothermal synthesis provides a simple mode of operation and the ability to grow large, high-quality crystals while maintaining a good control of their chemical composition [2]. Wu et al. successfully synthesized long range ordered uniform arrays of F-doped TiO_2 nanoflowers by a facile hydrothermal reaction of Ti foil with dilute HF acid [19]. Wang et al. prepared three-dimensional hierarchical anatase nanostructures with self-supported radially distributed nanoflakes, by hydrothermally treating Ti powder in the presence of H_2O_2 and NaOH, prior to an ion-exchange and calcination process. The growth process of the porous nanostructures was prompted by a self-organization process evoked by the Kirkendall effect and Ostwald ripening phenomenon [9,11,25]. A direct oxidation of metallic Ti foil using H_2O_2 solution under hydrothermal conditions was carried out by Wu et al. which yielded vertically-ordered titania nanorod thin film after annealing [13,14].

Herein, we present a facile one-pot hydrothermal method to prepare a hierarchical and mesoporous nanofungus-like anatase thin film. The as-prepared photocatalyst exhibited highly efficient photocatalytic degradation of Bisphenol A (BPA), an endocrine disruptor prevalently used as a precursor in manufacturing of polycarbonate plastic containers and epoxy resins, thus representing a significant advance in environmental remediation. This paper also provides a comparison between photocatalysts prepared under different hydrothermal durations, and aims to delineate a possible growth mechanism in obtaining the final nanofungus-like structure.

2. Experimental

2.1. Synthesis

Ti foils, each measuring 25 mm × 15 mm (99.7%, 0.25 mm thick, Goodfellow Cambridge Ltd, Cambridge, England) were first sonicated in acetone for 30 min to remove organic grime and washed with DI water. They were then etched in 20% HCl at 80 °C for 10 min to remove surface oxide layer, before thoroughly rinsed with copious amounts of DI water and finally dried in a N_2 gas stream. Each pre-treated Ti foil was then transferred to a 45 ml Teflon-lined autoclave (Parr Instrument, IL, USA), 75% filled with 30 wt.% H_2O_2 solution and 5% filled with 48 wt.% HF acid (Sigma–Aldrich). Caution! Hydrofluoric acid (HF) is extremely corrosive and toxic. HF must be stored in plastic vessels and carefully handled within a fume hood. The autoclave was then placed in an electronic oven that was maintained at 150 °C, for 3 h (labelled "NF3" in this manuscript); 5 h ("NF5"); and 10 h ("NF10"). After the hydrothermal treatment, the sample was left to cool under room conditions and subsequently washed carefully with DI water and dried in air. The sample was finally annealed in air at 450 °C for 1 h with a heating/cooling rate of 2 °C/min. All 3 of the resulting TiO_2 films are in the form of anatase and are firmly attached to the Ti substrate. For comparison purposes, a Ti foil was repetitively dip-coated in a Degussa P25 suspension to deposit a layer of homogeneous P25 nanoparticulate film on its surface. The suspension was prepared by dispersing 1.0 g of Degussa P25 TiO_2 powder in 20 ml of DI water, and then centrifuged to remove coarse and aggregated particles from the supernatant prior to the dip-coating process. The dip-coated foil was then air-dried at 120 °C for 30 min and the cycle was repeated continuously until an identical film weight across the 4 photocatalysts was achieved. The resulting sample is termed as "P25-coating".

2.2. Characterization

XRD analysis was performed using the Bruker Axs D8 Advance XRD (Bruker AXS GmbH, Karlsruhe, Germany) with monochromated high-intensity Cu Kα radiation ($\lambda = 1.5418$ Å) across a 2θ range of 5–80°, step size of 0.0040° and step time of 2 s. FESEM images were obtained using the JEOL 6340F FESEM (JEOL Ltd, Tokyo, Japan). The Oxford energy dispersive X-ray (EDX) spectroscopy detector used is a peripheral hardware equipped on the FESEM. High resolution TEM (HRTEM) and SAED micrographs were taken using the Jeol 2010F FETEM (JEOL Ltd, Tokyo, Japan), with an accelerating voltage of 200 kV. Prior to TEM analysis, a methanol suspension of the sample particles was spread on an amorphous carbon-coated copper grid. UV–vis diffuse reflectance spectra were obtained using Thermo Scientific Evolution 300 UV–vis Spectrophotometer (Thermo Fisher Scientific, MA, USA) equipped with an integrating sphere assembly and a Xenon lamp source. $BaSO_4$ was used as the reflectance standard and the spectra were converted from reflectance to absorbance. The porous structures of the respective samples were evaluated by N_2 adsorption–desorption isotherms using a Quantachrome Autosorb-1 system (Boynton, FL, USA) at −196 °C. The samples after calcination were first mechanically fractured by bending the Ti foils repeatedly until the overlaying anatase films peeled off from the Ti substrate. Under a controlled environment prior to analysis, the free-standing films were then grinded to fine powder using an agate mortar and pestle set. The Brunauer–Emmett–Teller (BET) approach using adsorption data over a relative pressure range was utilized to determine the specific surface area and porosity profile was estimated by the Barrett–Joyner–Halenda (BJH) method based on the obtained desorption curves. The samples were degassed at 150 °C to remove physisorbed gases before analysis. X-ray photoelectron spectroscopy (XPS) analysis was carried out at room temperature in an ultrahigh vacuum (UHV) chamber with a base pressure below 2.66×10^{-7} Pa. Photoemission spectra were recorded by Kratos Axis Ultra spectrometer (Shimadzu Corporation, Kanagawa, Japan) with a monochromatic Al Kα excitation source ($h\nu = 1486.71$ eV). Curve fitting was performed using a non-linear least square Gaussian–Lorenzian function with background subtraction by Shirley's algorithm. The binding energy (BE) scale was referenced and calibrated to the C 1s core level of the surface adventitious carbon at 248.8 eV.

2.3. Photocatalytic evaluation

Photocatalytic experiments were carried out separately in 5 identical glass bottles, each having a magnetic stirrer to induce homogenization and aeration during reaction. Prior to UV irradiation from a low-pressure UVP Pen-Ray mercury lamp (model no. 11SC-1L, UVP, LLC, California, USA), the catalyst sample (25 mm × 15 mm) was immersed in 15 ml of 20 ppm Bisphenol A (BPA, $C_{15}H_{16}O_2$) and stirred in the dark for 1 h to establish adsorption–desorption equilibrium. The initial concentration of BPA was then taken after 1 h of dark adsorption. The primary emission energy of the UV lamp was centred at 365 nm and typical light intensity was 1150 mW/cm^2. The lamp was placed inside each glass bottle at a fixed proximity to the catalyst to ensure that all samples receive an equal amount of UV irradiation. Photolysis experiment (without catalyst dosage) was performed under identical conditions over a blank Ti foil, also measuring 25 mm × 15 mm, to normalize the effect of BPA molecule adsorption on Ti substrates across the experiments. Removal rate of BPA was examined using a high-performance liquid chromatograph (HPLC, PerkinElmer Series 200). The HPLC analysis was carried out using an Inertsil ODS-3 column and a Series 200 UV–vis detector at 225 nm, with acetonitrile and water (70/30, v/v) as effluent at a flow rate of 1 ml/min.

All standard chemicals and scavenger solutions used in the experiments were prepared using reagent grade (99.9% purity) chemicals with DI water. All adsorption and photocatalytic oxidation experiments were carried out in triplicates (i.e. repeated three times) and the range of results was plotted in Figs. 8 and 9, as indicated from the error bars of each reading.

3. Results and discussion

3.1. Possible reaction pathways

The development of the hierarchical anatase nanofungus-like thin film structure is driven by the following reaction pathways based on the reactions of H_2O_2 and HF with Ti:

- When H_2O_2 reacts with Ti atoms on the foil surface, formation of titanium oxide layer (TiO_x) on the surface of the foil takes place due to the Kirkendall effect [9,26,27]. Under thermally activated conditions and because of differences in atomic diffusivities, interior Ti atoms tend to diffuse or migrate to the surface and react with H_2O_2 on the TiO_x/Ti interface based on the reaction below:

$$H_2O_2 + Ti \rightarrow H_2O + TiO_x \tag{1}$$

The Kirkendall effect commonly results in a highly porous structure of the titanium oxide layers due to directional matter flow and consequential vacancy accumulation [25]. Other reports have also shown that direct oxidation of metallic Ti foil using H_2O_2 would produce an amorphous hydrated titania porous film [28].

- HF serves not only to provide the F source, but also to etch the Ti substrate, providing a Ti source for further oxidation and formation of TiO_2 nanostructures. Therefore, the reaction of HF with Ti substrate is able to hydrothermally nucleate TiO_2 nanoparticles via a series of reactions as follows [19]:

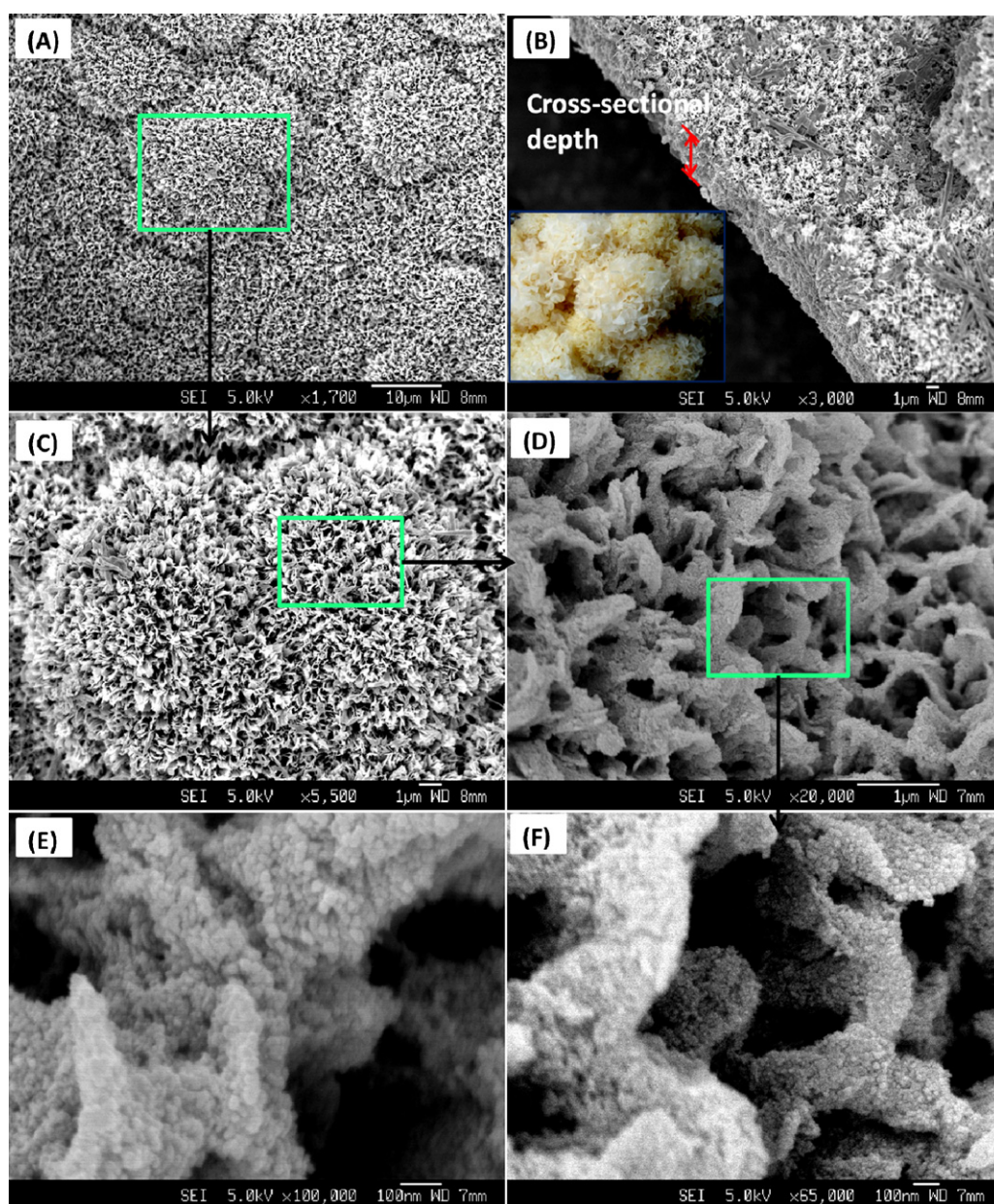$$Ti + 6HF \rightarrow H_2TiF_6 + 2H_2\uparrow \tag{2}$$

Fig. 1. FESEM images of nanofungus-like sample NF10, taken at different magnifications. Inset of (B): digital photograph of commercially available snow fungus.

$$H_2TiF_6 + 4H_2O \rightarrow Ti(OH)_4 + 6HF \quad (3)$$

$$Ti(OH)_4 \rightarrow TiO_2 + 2H_2O \quad (4)$$

- During the process of hydrothermal reaction, newly developed TiO_2 layer can gradually be dissolved by the HF solution to form TiF_4, resulting in thinning of the nanoflake walls [29]. It is known that HF is a corrosive chemical, hence the developed TiO_2 film may in turn be etched by HF as shown from Eqs. (5) and (6):

$$TiO_2 + 4HF \rightarrow TiF_4 + 2H_2O \quad (5)$$

$$TiO_2 + 6HF \rightarrow H_2TiF_6 + 2H_2O \quad (6)$$

The produced H_2TiF_6 species then diffuse to the exterior of the existing TiO_2 nanostructures already formed and new TiO_2 is repeatedly developed and aggregated on them, via reactions (3) and (4) [5]. The repeating cycles of dissolution and re-deposition result in the final mesoporous nanofungus-like structure [19]. It is noteworthy that calcination at 450 °C improves the crystallinity of the sample and converts the TiO_2 to an anatase polymorph, without causing noticeable morphological changes to the overall hydrothermally formed nanostructures.

3.2. Morphology

The structural features of the final product NF10 and the series of intermediate samples, NF5 and NF3, exhibited different topological morphology under different hydrothermal durations. From the overview FESEM image of NF10 sample in Fig. 1, densely packed 3D hierarchical microspheres with uniformly distributed nanoflakes, closely resemble commercial snow fungus commonly used as an ingredient in Chinese cuisine and medicine – photographed in the inset of Fig. 1B. Each spherical structure measured about 10 μm in width. The dense gelatinous-like appearance of the photocatalyst comprises of a flakey matrix façade that clump and overlap one another and each flake appear crisp at the edges. High magnification FESEM image from Fig. 1E and F reveal that the surfaces of nanoflakes are corrugated and covered with densely packed uniform primary nanoparticles of 20 nm. These nanoparticulates are primary building units and constituent components of the final nanofungus-like macrostructure; the driving force for their aggregation is likely associated with interfacial tension and van der Waals attractive forces [30–32]. Moreover, it has been reported that conventional hydrothermal synthesis compels slow convection within the autoclave, resulting in localized pockets of high concentrations of developed nanocrystallites, therefore promoting agglomeration [33].

As shown from the cross-sectional FESEM images of Fig. 1B, the nanofungus-like thin film has a depth of ca. 5–6 μm. The porosity and surface-to-volume ratios of the sample were greatly enhanced by these primary nanoparticles, which could induce efficient diffusion and mass transfer of organic pollutant molecules within the nanofungus architecture. The EDX spectra of NF10 (inset of Fig. 5A) showed that the spherical structures of TiO_2 were elementally composed of only pure Ti and O elements and no extraneous elements from intermediates were observed in the final anatase product.

NF5 displayed a nanostructure consisting of disuniformed self-supported stratified layers of radial nanoflakes. From the high resolution image, some of the nanoflakes were supported vertically and possessed a smooth surface, bearing resemblance to petals of a chrysanthemum flower. The emanated flakes are ultrathin, with thicknesses of only a few nanometers and are broad-spanned with widths of ca. 100–200 nm. NF3, on the other hand, was noted with presence of random and disordered nanoflake-like structures over its continuous film. Occasional small cavities that seem gradually eroded within the underlying nanofibrous network were noticed

from Fig. 2C. High magnification FESEM image from Fig. 2D, illustrates that the observed nanoflake-like structures, each spanning up to a few micrometers, were constructed by bunching and clustering of nanowires (widths of 10–20 nm).

As shown from the morphology of NF3 and NF5, the nanoflake structure was constructed by coalescence of nanofibres formed after 5 h of hydrothermal reaction. Under a hydrothermal environment, the primary nanoparticles were crystallized on the solid–liquid interface via a dissolution–precipitation mechanism, leading to nucleation and growth of anatase nanoparticles on the nanoflake structure. This mechanism is analogous to our recently reported hydrothermal synthesis of $SrTiO_3$ crystallites on TiO_2 nanowires [4]. Since no discernible discrepancy in size was observed with the primary anatase particles on the nanoflake structure, the hydrothermal reaction mechanism proceeded in good agreement with the classic LaMer model [34]. The results from Figs. 1 and 2 demonstrate that a longer hydrothermal reaction (10 h) with HF precursor has resulted in a progressively hollowing effect in its interiors, as indicated from the rough external façade of nanoflakes and the presence of mesopores from intraparticulate voids. This is caused by dissolution of amorphous components as well as interiors of the structural framework via an etching effect of F^- in acidic conditions. Furthermore, Yu et al. pointed out that the hydrogen bonding and surface absorption of F^- reduces attenuation of electrostatic repulsion, thus mobility of protonated TiO_6 octahedra and mass transfer from within the nanofungus structure to the bulk solution are significantly enhanced [35]. In general, construction of the overall nanofungus-like morphology was driven by a coupled process of fluoride-mediated self-transformation and localized Ostwald ripening, where interior nanoparticles are selectively dissolved and new nanocrystals are crystallized and precipitated on the surfaces of the nanoflake stratification. On the other hand, NF5 possessed a solid, clean and smooth surface of nanoflakes as seen from Fig. 2B. The absence of mesoporous intraparticle voids explains its lower specific surface area and macroporous structure. In the case of NF3 where coalescence of neighbouring short, broken nanofibres was evidenced in Fig. 2D, specific surface area was recorded to be smallest among the 4 samples. Wu et al. reported such a trend as a result of crystal grain growth during coalescence of neighbouring nanoparticles, therefore notably reducing specific surface area of condensed titania films [14].

It should be noted that after 10 h, there was no discernible change in terms of morphology of the nanofungus-like structure, suggesting that a critical equilibrium state has been reached. Moreover, a lengthier hydrothermal duration beyond 10 h would result in poor mechanical strength of the film and weak adhesion to the Ti substrate. Due to natural capillary action and surface tensional forces, the overlaying film tends to curl and fracture into shards upon drying in air (shown in Fig. S1), thereby posing a significant problem for constructive applications. This may be engendered by anisotropic growth of nanoparticles in different crystallographic directions over a prolonged crystallization reaction, resulting in a thick depth of film. Henceforth, mechanical stability and adhesion to the underlying Ti substrate were compromised as a result of surface tension acting on the liquid–air interface.

From Fig. 2E, it is evident that the P25 coating consist of solid primary nanospherical particles measuring ca. 25 nm each and the film coating recorded a specific surface area of 52.2 m^2/g. Both figures were consistent to manufacturer's product specifications of commercial Degussa P25. Some remote clusters of aggregated P25 nanoparticulates were also observed among the nanospheres, which was expected after the repeated dipcoating and heat treatment process. The overall coating was uniform and well dispersed on both sides of the Ti foil.
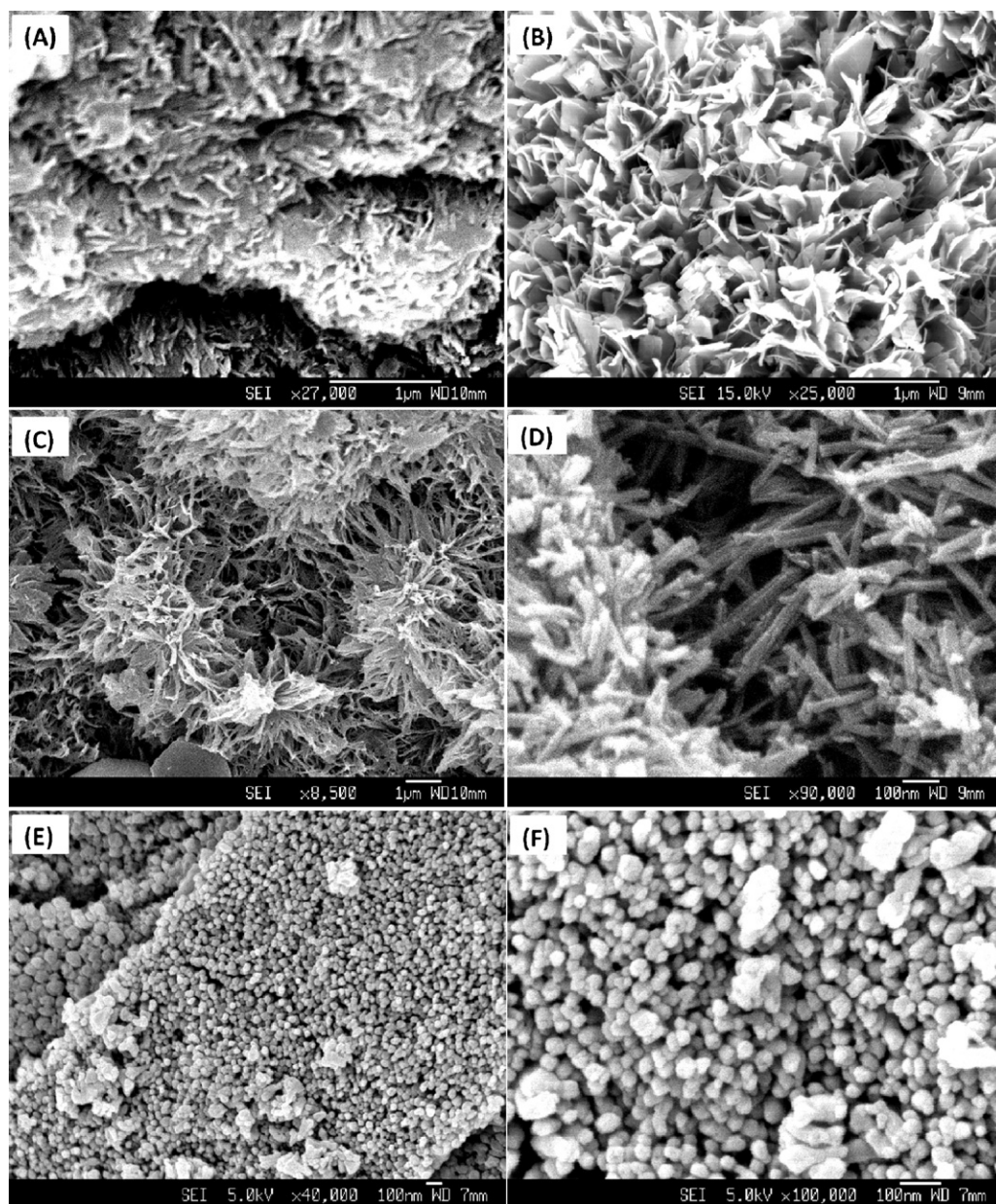
Fig. 2. FESEM images of (A and B) NF5 sample, (C and D) NF3 sample, (E and F) P25 coating sample.

3.3. Surface elemental analysis

XPS survey spectra of NF10 in Fig. 3 manifest that the surface of the sample contains Ti, O and C elements. No other impurity elements, except C, are present. The small C 1s feature at 284.8 eV is attributed to residual carbonates and adventitious hydrocarbon following contamination from air exposure and the XPS instrument [36,37]. However, due to the low concentrations of residual F in the thoroughly washed sample after calcination, EDX and the wide scan XPS analysis were unable to distinguish the origin of F signal. In order to decipher the F signal, a high resolution XPS spectrum of the F 1s region of NF10 was measured and presented in Fig. 3. The high resolution scan evidenced the extent of HF etching that was consonant with XRD results, since NF10 was recorded to possess the smallest crystallite size (10.2 nm) among the other samples [38]. The main feature from the high-resolution XPS spectra of the F 1s region was centred at 684.6 eV, which corresponds to the surface fluoride ($\equiv$Ti–F) originating from ligand exchange between F$^-$ anions and surface hydroxyl group on TiO$_2$ [37,39]. This is attributable to F$^-$ ions physically adsorbed on the surface of TiO$_2$ [40]. Contrary to nucleophilic substitution of F$^-$ ions and titanium alkoxide during hydrolysis, absence of feature around 688.5 eV indicates that no signal of substituted F$^-$ ions in the lattice of TiO$_2$ was detected [40–42]. Although, the atomic radii of F$^-$ and O$_2{}^-$ ions are similar, the low relative concentration of F$^-$ ions and hydrothermal temperature (150 °C) applied was insufficient to trigger substitution of F$^-$ for O$_2{}^-$ in the lattice. Moreover, Yu et al. has also reported that surface fluorination of TiO$_2$ is more inclined to take place in an acidic hydrothermal environment thus preventing interstitial substitution of F$^-$ for O$_2{}^-$ in the lattice of TiO$_2$ [41]. The hydrothermal environment, via an in situ dissolution–precipitation process, has been reported to expedite crystallization of TiO$_2$ with reduced defects and impurities, also shown from the TEM and EDX results of Fig. 5 [4,43]. Henceforth, although the hydrothermal temperature was relatively low, our acidic hydrothermal synthesis was able to yield surface-fluorinated anatase TiO$_2$.
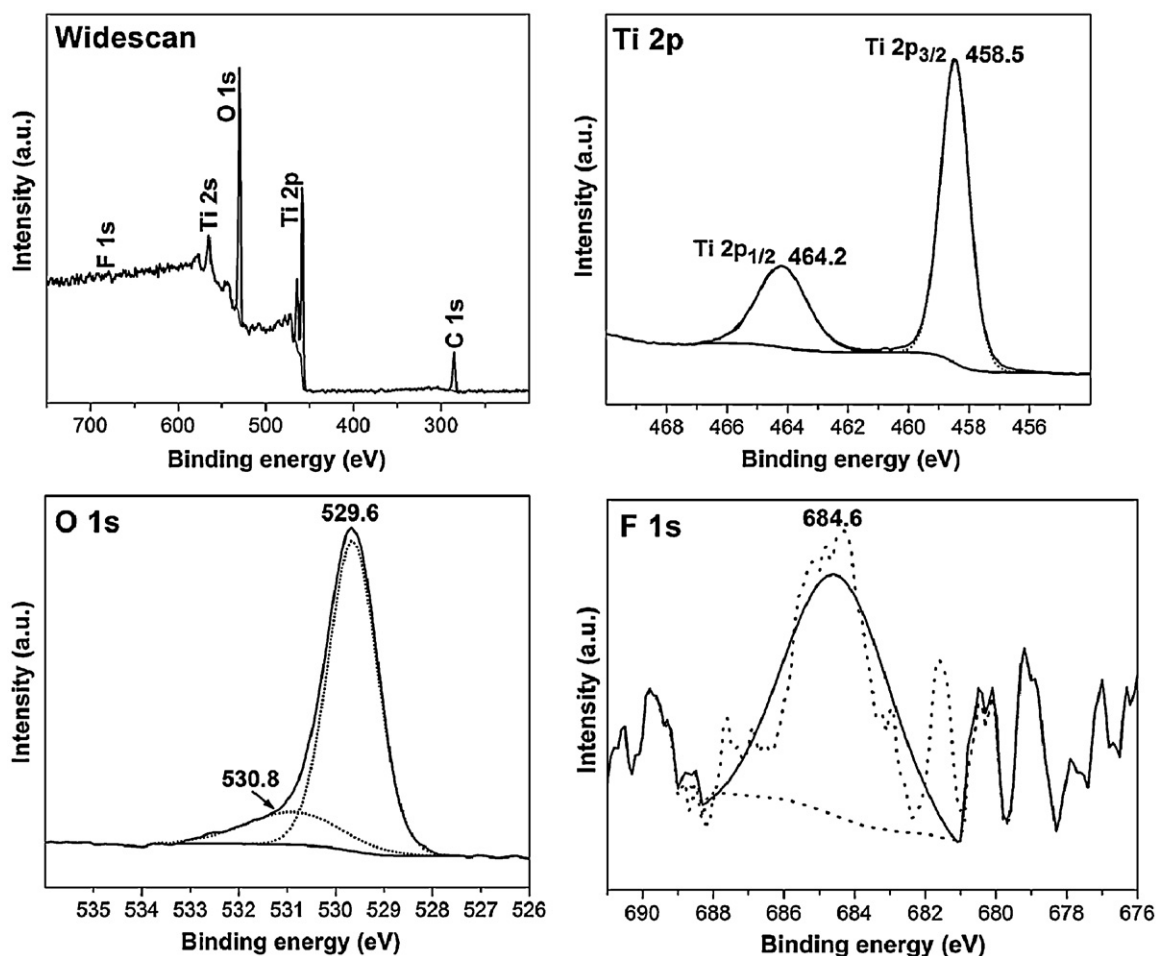
Fig. 3. XPS survey spectrum of NF10 sample and its corresponding high-resolution XPS spectra of the Ti 2p, O 1s and F 1s regions.

Observations from high resolution XPS spectra of Ti 2p reveal 2 clear features, Ti $2p_{1/2}$ and Ti $2p_{3/2}$, centred respectively at 464.2 eV and 458.5 eV. Based on previous literature and XRD results, these peaks originate from the presence of TiO_2 [36,44,45]. No other peaks from partially oxidized Ti^{2+} or Ti^{3+} were detected. The curves of O 1s region can be deconvuated into 2 peaks at 529.6 eV and 530.8 eV, both of which can be assigned to TiO_2 as well [36,45]. The first O 1s peak is inherent from O atoms bounded to metals, such as Ti [46], while the latter peak reveals possible surface contamination by hydroxyl species [4]. It is noteworthy that the high resolution XPS spectrum of F 1s region was absent in samples NF5 and NF3, possibly due to the much shorter hydrothermal reaction time with HF precursor. Additionally, the high resolution Ti 2p and O 1s XPS spectra of NF5 and NF3 were very similar to those of NF10, further confirming formation of pristine TiO_2 in the absence of fluoride.

3.4. Crystallographic phase and orientation

Fig. 4 compares the XRD spectra of the 4 samples. As the film samples are embedded on a Ti foil, Ti (JCPDS no. 89-5009) peaks can be indexed to every spectrum. Well resolved and sharp peaks of TiO_2 body-centred tetragonal anatase phase (space group: $I4_1/amd$ (141); measured lattice constants of $a_o = 3.785$ Å and $c_o = 9.514$ Å; JCPDS no. 21-1272) are evidently present in all 4 samples, with 2θ values of 25.3°, 48.1°, 53.9° and 55.1°, indexed to the (1 0 1), (2 0 0), (1 0 5) and (2 1 1) peaks respectively. The anatase phase of TiO_2 has been reported to possess a higher photocatalytic efficiency as compared to the rutile phase [47], largely due to the close

packing structure of the rutile polymorph, which resulted in a lower surface area [48]. Electron transfer within the anatase phase is also relatively faster than in the rutile phase, since the anatase phase possesses higher conduction-band edge energy [49].

It is apparent that the XRD peaks of NF3 are relatively weaker possibly due to the short hydrothermal duration (3 h) that may
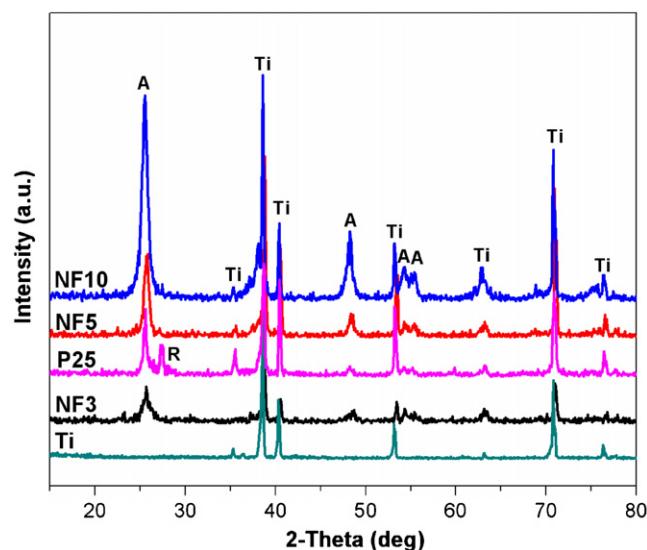

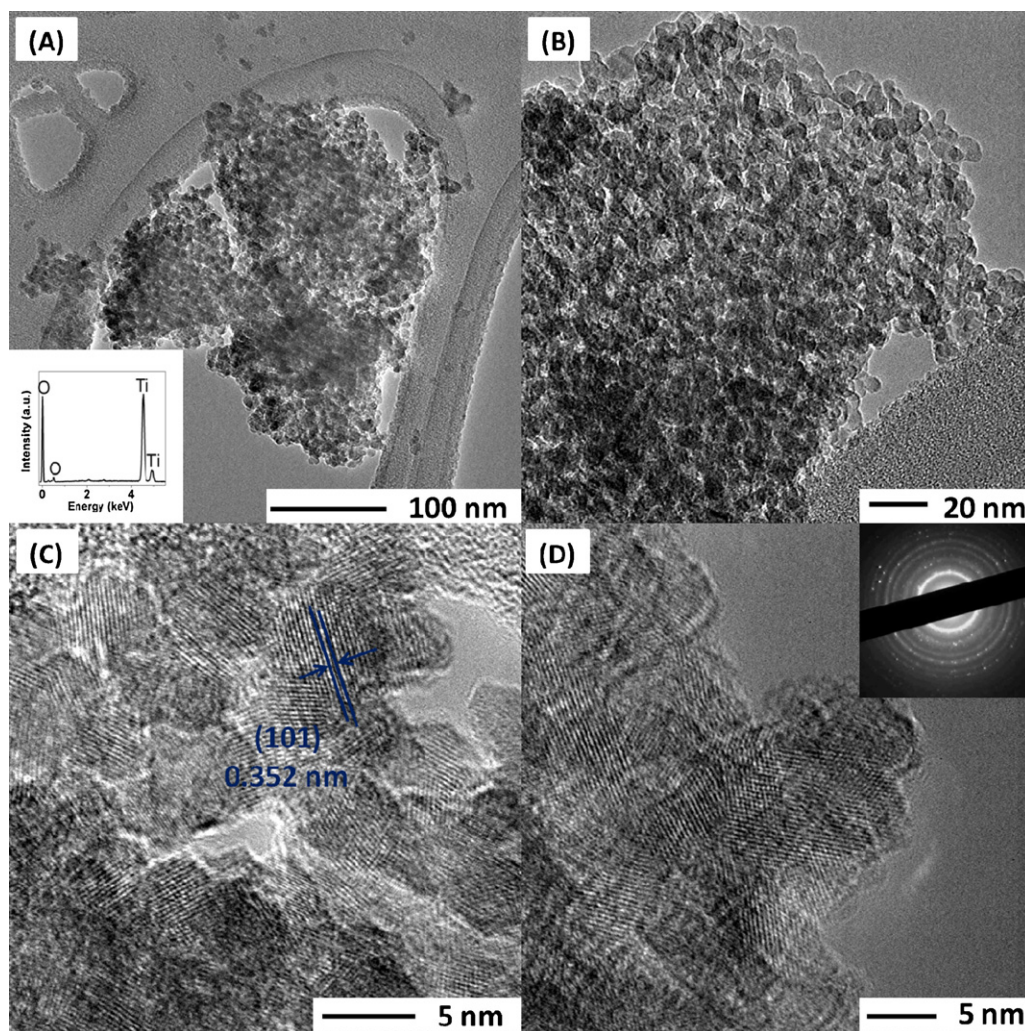**Fig. 4.** XRD spectra of the as-prepared photocatalysts.

Fig. 5. (A and B) Typical TEM micrograph of the ultrasonic-dispersed NF10 sample, inset of (A): EDX spectra of NF10; (C and D) HRTEM showing crystal lattice orientation and interplanar distance, inset of (D): corresponding SAED pattern of NF10.

have led to an incomplete growth of the crystal structure. No peaks of the rutile or brookite phase were detected in the XRD spectrum of the hydrothermally prepared samples of NF10, NF5 and NF3, indicating the high purity of anatase polymorph after calcination. The respective anatase crystallite sizes was calculated based on Scherrer Equation [50] and the P25 coated sample reveals an anatase crystallite size of *ca.* 20 nm, consistent with reported literature [51]. Calculated anatase crystallite sizes of the photocatalysts are tabulated in Table 1. Apart from recorded anatase phase, the rutile polymorph (JCPDS no. 21-1276) with a pronounced peak at $2\theta = 27.4°$ of the (1 1 0) reflection, can be indexed from the XRD patterns of P25 coating on Ti substrate. This was expected since commercial P25 consists of a mixed phase of anatase and rutile in the ratio of *ca.* 4:1 [52]. The enhanced intensity of the

predominant (1 0 1) reflection centred at $2\theta = 25.3°$ across all 4 samples, indicates a thermodynamically stable (1 0 1) plane of the body-centred tetragonal anatase polymorph. In addition, it has also been widely reported that the (1 0 1) plane possess the lowest surface energy and thus most energetically stable [53]. Therefore, judging from intensity of the respective (1 0 1) peaks, the magnitude of crystallinity follow the order of NF10 > NF5 > P25 coating > NF3 and incidentally, it is consonant to the order of photocatalytic activity, suggesting that crystallinity of a sample is an essential property to its photoactivity. From the substantially higher and sharper XRD diffraction peaks of NF10, it can be observed that the longest hydrothermal duration (10 h) yielded strongest crystallinity. This result re-establishes the fact that anatase crystallite growth

Table 1
Physicochemical properties of the synthesized anatase nanofungus-like thin film photocatalysts.

Photocatalyst	Anatase size[a] (nm)	Specific surface area (m²/g)	Average pore diameter (nm)	Total pore volume (cm³/g)	Indirect bandgap (eV)	Film weight ± 0.05 (mg/cm²)	Photocatalytic activity, k (min⁻¹)
NF10	10.20	102.1	7.5	0.38	3.07	1.182	0.053
NF5	11.92	63.2	12.3	0.67	3.12	1.097	0.018
NF3	11.04	34.5	25.6	0.19	3.22	1.073	0.008
P25-coating	21.21	52.2	11.8	0.245	3.17	1.127	0.013

[a] Calculated based on the (1 0 1) peak for anatase, according to the Scherrer Equation.

was enhanced and lesser critical nuclei were formed in the presence of F$^-$ ions, thus sufficient nutrients were available to promote anatase crystallization within the hydrothermal environment [35,40].

The TEM results of NF10 show dispersed primary nanoparticles after subjecting the sample to intensive ultrasonication in methanol prior to TEM analysis. It can be hypothesized that intraparticulate voids between these aggregated primary nanoparticles can create accessible hollow channels for increased surface area of reaction and optimized UV light penetration from the exterior. From TEM micrographs of Fig. 5, it is apparent that the constituent components of the NF10's nanofungus structure reveal certain aggregated masses of nanoparticles with occasional arch-shaped and undulating, protruding features (Fig. 5D) that were inherent from both the nanoflake and nanofungus-like structures – consistent to FESEM images. Fringe lattices were readily distinct from corresponding high resolution TEM (HRTEM) images of NF10, implying that the sample was well crystallized after calcination. From Fig. 5C and D, it is evident that lattice characteristics reflect broken crystal fringe lattices to the edge of the sample, with presence of grain boundaries at overlapped interfaces of aggregated nanocrystallites – an indication of polycrystallinity. The inset of Fig. 5D yields a selected area electron diffraction (SAED) pattern of NF10 which shows a series of concentric rings, thereby affirming the polycrystalline complex of NF10. The diffraction rings are composed of discrete spots which indicates that the matrix material consists of a small number of rather large crystallites, possibly from agglomerated crystallites. Applying the Bragg's Law and assuming that Bragg's angles are very small (*ca.* 1°) in diffraction of fast electrons, the interplanar spacings and corresponding lattice planes diffracting the beam can be calculated and identified respectively [54]. The four most distinct concentric diffraction rings, starting from the inner ring nearest to the centre electron beam, can be sequentially assigned to (1 0 1), (2 0 0), (1 0 5) and (2 1 1) diffraction planes of the body-centred tetragonal structure of anatase TiO$_2$ [20]; a result in agreement with the observed XRD spectrum of NF10 (Fig. 4). A parallel linear marking that measures an interplanar d-spacing of 0.352 nm between the planes of atomic lattices parallel to the (1 0 1) planes was highlighted in Fig. 5C. This demonstrates a preferential crystallographic growth of nanoparticles along the (1 0 1) crystal plane with a preferred orientation in the [0 1 0] direction.

3.5. Optical spectrum analysis

Fig. 6 presents the UV–vis diffuse reflectance spectra of the synthesized photocatalysts. The inset of Fig. 6 is plotted by application of the transformed Kubelka–Munk theorem, of $(\alpha h\nu)^{1/2}$ against $h\nu$, and a straight line tangential to the vertical segment of the slope is extended to intersect the $h\nu$ axis (*x*-axis) in obtaining the indirect bandgap (E_g) value of the samples [55]. The synthesized photocatalysts show marked absorption at wavelengths shorter than 400 nm that can be ascribed to intrinsic bandgap absorption of pure anatase TiO$_2$. [56]. In comparison to the other samples, absorption edge of NF10 red-shifted in the bandgap transition, implying that F$^-$ doping (observed from XPS results of NF10) results in narrowing of bandgap – a phenomenon that is widely agreed upon from literature [38,40,41,57]. It is also worthy to note that among the 4 photocatalysts, NF10 exhibited the strongest absorption response across a UV–visible range of 250–650 nm. The observed trend may be attributed to enhanced light harvesting properties: high specific surface area associated with corrugated nanoflake surfaces and accessible mesoporous voids of the hierarchical nanostructured framework permit light penetration and scattering within the interior of the catalyst morphology. The increased UV photons are expected to produce additional photogenerated electron–hole
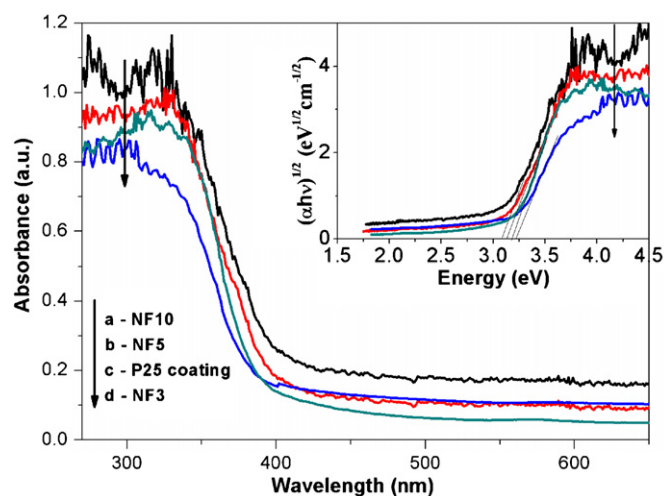

Fig. 6. UV–vis diffuse reflectance spectra of the as-prepared photocatalysts. Inset: corresponding Kubelka–Munk transformed reflectance spectra.

pairs and oxidizing radicals to participate in photocatalytic reactions, therefore improving photocatalytic activity of NF10 [58]. In addition, the steepest absorption band of NF10 among the 4 samples, as well as the presence of minor exciton peaks at around 320 nm, serve to suggest that the TiO$_2$ nanocrystals of NF10 are highly uniform in size and shape [59].

From Table 1, the indirect bandgaps of anatase-TiO$_2$ samples (NF10, NF5 and NF3) were in the range of 3.07–3.22 eV; consistent to reported bandgap values of bulk anatase TiO$_2$ [56]. Absorption edge of NF10 was shifted towards longer wavelengths, thus resulting in the decrease of bandgap energy due to the combined effects of several factors, such as enhanced light harvesting abilities, presence of accessible mesopore voids and surface fluorination. Despite having the same anatase crystalline phase, it has been reported that morphology of semiconductor materials exercise a certain extent of influence on characteristic light absorption properties and can hence, alter the intrinsic electronic band structure [60].

It is worth noting that absorption onset of the hydrothermally prepared photocatalysts was observed at around 400 nm, similar to the P25 coated sample which was prepared without F precursor. This exemplifies the fact that absorption edge region was unaffected from the extent of surface fluorination [40]. The result is also consistent with high resolution XPS spectra of F 1s region that F element did not enter the lattice of TiO$_2$ [41].

3.6. Porosity and textural properties

Fig. 7 shows the N$_2$ adsorption–desorption isotherms of the photocatalysts. The isotherms of the scratched off P25 coated film and NF3 can be classified as Type III, with the adsorption and desorption curves coinciding, i.e. no hysteresis loop was observed. This illustrates that the samples are non-porous, and is in good agreement with reported isotherm of P25, since it is known that Degussa P25 is a type of non-porous powder formed by a mixture of anatase and rutile polymorphs [61–63]. Taking into account the absence of nitrogen adsorption at low pressures, it can be concluded that micropore contribution to the total pore volume was negligible for both P25 and NF3 samples. As seen from their isotherms, adsorption curves gradually increased in the middle-pressure region and exhibited an abrupt hike across the high-pressure region ($P/P_o > 0.8$), hence adsorption behaviour of the samples can instead be attributed to capillary condensation and multilayer adsorption of nitrogen in macropores [62]. On the other hand, the adsorption–desorption
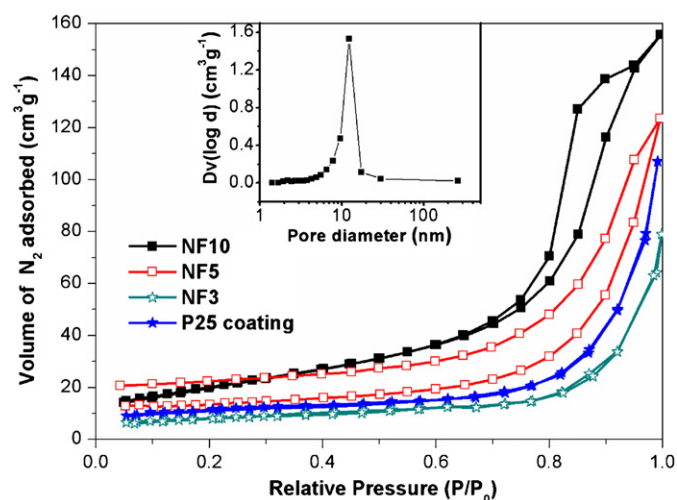
Fig. 7. Nitrogen adsorption–desorption isotherms of the as-prepared photocatalysts. Inset: corresponding pore size distribution of NF10.

isotherm of NF5 is categorized under Type II, indicative of a macroporous sample with unrestricted monolayer–multilayer adsorption. The almost linear middle part of the curve represents the completion of monolayer coverage where multilayer adsorption would commence subsequently [64].

According to IUPAC classification [64], NF10 exhibited Type IV nitrogen isotherm with a Type H1 hysteresis loop, which is associated with the secondary process of capillary condensation and resulting in the complete filling of mesopores at $P/P_o < 1$ [65]. As with most mesoporous TiO$_2$ samples, the adsorption of NF10 would proceed as multilayer adsorption initially before capillary condensation takes over as the dominant adsorption mechanism [63]. With reference to the 3 other isotherms from Fig. 7, adsorption trend of NF10 at low-pressure region appears to be similar initially, but with increase of relative pressure, uptake of N$_2$ increases sharply due to capillary condensation within the mesopores of NF10. The observed hysteresis loop between adsorption and desorption isotherms of NF10 was developed due to discrepancies in the rates of capillary condensation and evaporation. The two branches from the hysteresis loop are almost vertical and nearly parallel over a considerable range of gas uptake across a pressure region of $0.8 < P/P_o < 0.95$ – characteristic of the H1 hysteresis loop [64]. It can be observed from Fig. 7 that the monolayer adsorption of mesoporous NF10 was only completed at a relative pressure of 0.7, implying abundance of mesopores within the NF10 sample. From the FESEM images, the primary nanoparticles were in uniform sizes of *ca.* 20–40 nm, henceforth, mesoporosity of NF10 may be imparted by intraparticulate voids within pores of these nanoparticles, rather than the gaps between these particles (interparticulate voids). TEM results signify that the nanoparticles act as conjugate building blocks of the overall nanofungus morphology, henceforth the pores may be connected to other pores in forming an interconnected porous network.

Since the IUPAC guidelines recommend that the computation and interpretation of mesopore size distribution is valid only for Type IV isotherms [64], pore size analysis of only sample NF10 was plotted in the inset of Fig. 7. The sharp peak centred at the pore diameter of 10 nm is in good agreement with our assertion that the mesopores were inherent from internal pores (intraparticle pores) of the primary nanoparticles, and that NF10 is characteristic of solids crossed by channels of uniform sizes and shapes. The narrow pore size distribution curve provides evidence that the sample contains mesopores (2 nm < pore size < 50 nm) with a high degree of uniformity and geometry.

It is generally accepted that an increased surface active sites offers positive effects to surface-based processes, such as heterogeneous photocatalysis, by improving adsorption efficiency [13,14]. Mesopores of NF10 aid in facilitating rapid diffusion and transport of molecules via an interconnected porous network, and enhance harvesting of UV light from a large surface area by multiple scattering within the porous framework [35,66,67]. It is noteworthy that in general, internal pores will be much smaller in size and volume than voids between particulates, but they often provide dominant contribution to the total surface area of the solid [68].

The specific surface area and pore volume of the samples are tabulated in Table 1. Obviously, NF10 possessed the largest surface area of 102.1 m^2/g, in comparison to P25 (52.2 m^2/g), NF5 (63.2 m^2/g) and NF3 (34.5 m^2/g). The active surface sites, related to BET surface areas, were important for the adsorption of pollutants and desorption of product molecules.

3.7. Dark adsorption

The adsorption of BPA over the synthesized photocatalysts without light irradiation was examined in detail. Difference in adsorption capacity can be correlated to the specific surface area and porosity of the photocatalysts. It is apparent from Fig. 8A that the extent of BPA adsorption in dark was insignificant; less than 2% of BPA was removed after 60 min of dark adsorption. This can be attributed to a relatively high concentration of BPA (20 ppm) applied in our study while only a small dosage of photocatalyst (*ca.* 4 mg in 15 ml of aqueous BPA) was employed. BPA molecules, with respective pK$_{a1}$ and pK$_{a2}$ values of 9.6 and 10.2, consist of two negative oxygen atoms at the hydroxyl groups and four negative carbon atoms ortho to the phenolic group [69]. In our study, pH of BPA solution was not adjusted and hence maintained at *ca.* 6.7–7.0. On the other hand, TiO$_2$ is known to be amphoteric in aqueous solution and anatase TiO$_2$ has a point of zero charge of pH 5.9 [13], thus the photocatalysts were negatively charged in BPA solution. At higher pH values ≥ 7, deprotonation of BPA molecules to form BPA$^-$ and BPA^{2-} ions is expected to occur, leading to repulsion from the negatively charged TiO$_2$ surface. In addition, it is noteworthy that highly oxidative peroxo complexes coordinated to Ti(IV) are formed from the reaction of Ti and precursor H$_2$O$_2$ [28]. The abundance of such superoxide groups in TiO$_2$ resulted in an even more negatively charged photocatalyst surface, which readily repelled BPA molecules at pH 7, leading to its poor adsorption affinity. However, the strong oxidative power of these complexes would accelerate photodecomposition of organic compounds via direct oxidation, or by surface-trapping photogenerated holes to produce reactive oxygen radicals (to be discussed in the later section) that are primarily responsible in the oxidation of BPA.

The Langmuir–Hinshelwood model was applied to model the rate of BPA disappearance [69]:

$$r = -\frac{dC}{dt} = k\left(\frac{KC}{1 + KC}\right) \qquad (7)$$

where r is the rate of BPA disappearance (mg/(L min)) and C (ppm) is the BPA concentration. K represents the equilibrium constant related to monolayer adsorption and k is the reaction rate constant which represents a good measure of the samples' photoactivity.

$$\frac{1}{r_o} = \frac{1 + KC_o}{kKC_o} = \frac{1}{kK} \cdot \frac{1}{C_o} + \frac{1}{k} \qquad (8)$$

The constants, k and K, were determined from a plot of $1/r_o$ against $1/C_o$, with the slope being $1/(kK)$ and the intercept as $1/k$. To establish a better understanding of BPA adsorption behaviour on NF10, experiments of BPA photodegradation were carried out at different initial concentrations from 5 to 40 ppm. The empirical and calculated results are shown in Table 2. Applying the kinetics results
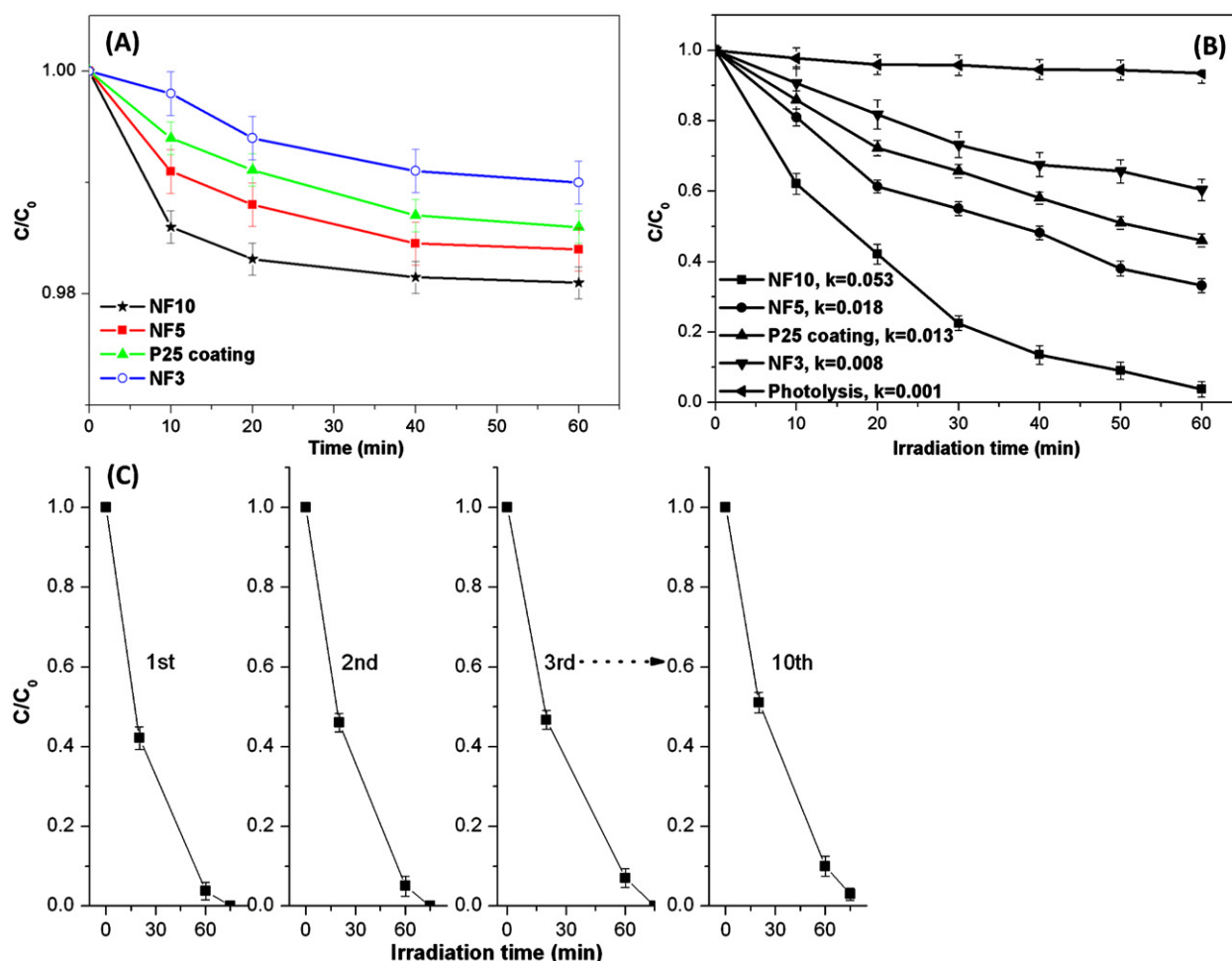
Fig. 8. (A) Change in BPA concentration over dark adsorption for 60 min; (B) photodegradation of 20 ppm BPA in the presence of NF10, NF5, NF3, P25 coating and Ti substrate (photolysis), obtained from an average of three runs, the error bar reflects root-mean square deviations of the values from each run; (C) irradiation–time dependence of the relative concentration C/C_o of BPA in solution over NF10 during repeated photooxidation experiments, from cycle 1 to cycle 10, under UV irradiation.

above generates a highest KC value of 0.14 at the initial stage of reaction when $C = C_o$. In addition, BPA concentration, C, would decline sharply as reaction proceeds with time due to ongoing photodegradation. Therefore in general, the KC term can be deemed negligible ($KC \ll 1$) and the kinetics equation can be further simplified to follow a pseudo first order expression in Eq. (9), which is in good agreement with the observed exponential trend of Fig. 8B.

$$-\ln \frac{C}{C_o} = kt \qquad (9)$$

where C is the BPA concentration at stated time, t, C_o is the initial BPA concentration measured after 1 h of dark adsorption and t is the reaction time.

3.8. Photocatalytic evaluation

As shown in Fig. 8B, photocatalytic degradation trend of BPA is presented as BPA concentration against irradiation time. NF10 recorded the highest photocatalytic activity ($0.053\,\text{min}^{-1}$), by a factor of almost 3 times than that of NF5, which exhibited 2nd highest activity ($0.018\,\text{min}^{-1}$). The P25 coated sample, due to its highly-crystallized state and large specific surface area in nanoparticulate form, recorded the next highest activity at $0.013\,\text{min}^{-1}$. NF3 yielded the lowest photocatalytic activity ($0.008\,\text{min}^{-1}$), almost 6 times poorer than NF10. Due to the photostable nature of BPA, photolysis experiments performed under UV-A irradiation for 60 min, only led to a negligible concentration reduction. Each Ti foil was weighed before and after synthesis to determine the respective mass of film developed on the foil. Film weight variance was less

Table 2
Empirical data derived from photocatalytic degradation of BPA at different initial concentrations.

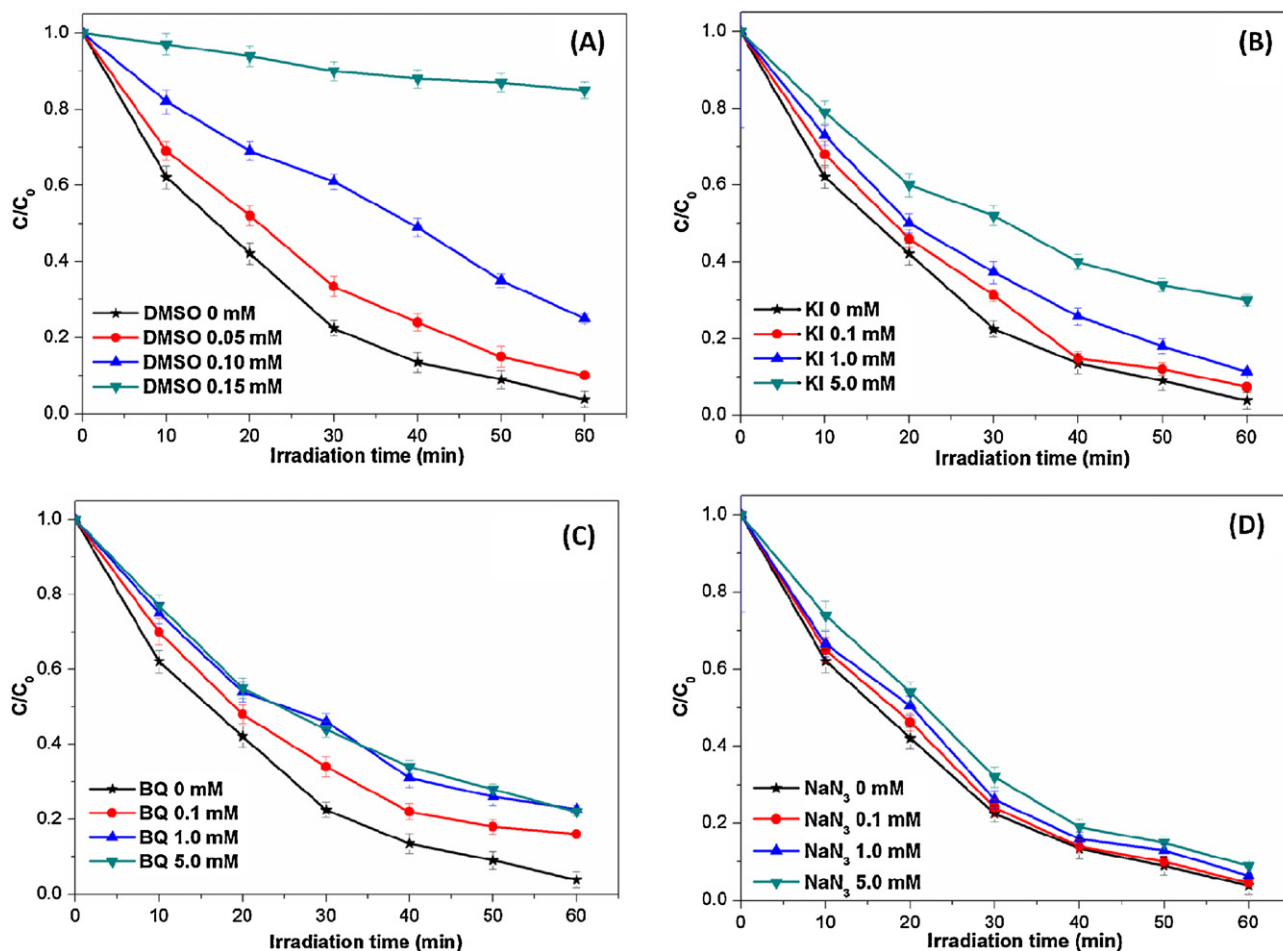| BPA initial concentration, C_o (ppm)	Initial reaction rate constant, k (min^{-1})	Initial reaction rate, r_o ($\text{ppm}\,\text{min}^{-1}$)	Adsorption constant K (L/mg)	R^2
5	0.055	0.275		
10	0.053	0.53		
20	0.053	1.06	0.007	0.988
30	0.047	1.41		
40	0.045	1.8		

Fig. 9. UV-photocatalytic degradation of BPA over NF10 under the interference of (A) DMSO; (B) KI; (C) BQ; (D) NaN₃.

than 10% across the 4 samples, therefore rational comparison of photoactivities between the photocatalysts can be established.

Fig. 8C plots the photocatalytic removal percentage of BPA by sample NF10 over 10 repeated cycles of usage. After each photocatalytic reaction cycle of 75 min, the same sample of NF10 was transferred into a fresh (20 ppm) solution of BPA to undergo reaction at identical conditions. It is apparent that 100% of BPA degradation was attained after 75 min of reaction and after 10 cycles of continuous usage, photocatalytic efficiency only dipped slightly to 98% but was conveniently restored to 100% after an additional 5 min of UV exposure to the sample. In addition, there was no distinctive change in the surface morphology of NF10 after 10 cycles of reuse, exemplifying the highly stable nanofungus-like structure.

The strong electronegativity of fluorine present on the surface of NF10 has been proven to trap photogenerated electrons and prevent recombination with photogenerated holes [57], therefore increasing production of free •OH which could explain the accelerated photocatalytic degradation of BPA. Minero et al. reported that fluorinated surface promotes generation of free mobile •OH while majority of •OH produced from pristine TiO₂ tend to remain adsorbed on the surface [39]. Increased concentration of •OH generated by F-TiO₂ under UV illumination has also been confirmed by direct spin-trapping electron paramagnetic resonance measurements [70]. Additionally, desorption and transport of •OH induced by surface fluorination can also enhance remote photocatalysis at the air/catalyst interface.

Walker et al. [71] proposed that a highly porous photocatalyst will retard transportation of photogenerated intermediates within its pores and impede diffusion into the bulk solution, thus

increasing their likelihood of being further oxidized and mineralized. Henceforth, it is not unreasonable to postulate that the unique mesoporous nanofungus-like morphology with large surface area have contributed positively to enhancing photocatalytic activity. Furthermore, the corrugated and highly porous nature of NF10 provides access for UV light to scatter and irradiate inner folds of the thick and porous framework, generating higher concentration of active radical species in the process.

3.9. Photocatalytic reaction mechanisms

Photocatalytic degradation of BPA via NF10 was intervened by addition of radical scavenging species, such as dimethyl sulfoxide (DMSO), potassium iodide (KI), benzoquinone (BQ) and sodium azide (NaN₃) to investigate contributory roles of the respective generated reactive oxygen species in hydroxyl radical •OH, photogenerated hole h⁺, superoxide radical $O_2^{\bullet-}$ and singlet oxygen $^1O_2$. Upon UV activation of the photocatalyst, photogenerated electrons are quenched by surface chemisorbed oxidants to produce oxidative radicals. Chemisorbed oxidants usually exist in the form of dissolved dioxygen, which serve as electron scavengers to hinder electron-hole recombination. Although hydrogen peroxide (H_2O_2) is generated during reduction of dioxygen, its impact was not studied since oxidative potential of H_2O_2 is much weaker as compared to the investigated radicals. Subsequently, active oxygen species were believed to first diffuse into the bulk solution from the photocatalyst and then participate in oxidative reactions within the homogeneous phase. As shown from Fig. 9, it is clear that the degradation of BPA was driven predominantly by •OH, followed by h⁺ and

$O_2{}^{\bullet-}$, while the role of $^1O_2$ in BPA degradation was found to be least critical.

Fig. 9A shows that parallel to the increment of DMSO concentration, an obvious decline in BPA photodegradation was observed and the inhibitory effects were accentuated with increasing DMSO concentration. When 0.15 mM DMSO was added to quench free $^\bullet$OH in the system, photocatalytic efficiency was drastically impaired by 85.6% as the consumed $^\bullet$OH can no longer perform oxidative radical attack on BPA molecules. This is a clear indication that a high yield of $^\bullet$OH was generated in the UV/TiO$_2$ system and exemplifies the pivotal role of $^\bullet$OH as the predominant species behind UV-photocatalytic removal of BPA. Moreover, since $^\bullet$OH generated on fluorinated surfaces of TiO$_2$ (NF10) are more mobile than those generated on pristine TiO$_2$, inhibition of BPA degradation was more pronounced with the addition of DMSO, in comparison to scavengers of other reactive oxygen species [42].

In the presence of increasing KI concentration, photocatalytic oxidation of BPA was noted to attenuate. The quantitative analysis of I$^-$ oxidation connote that photogenerated h$^+$ play an intermediary role in photocatalytic degradation of BPA via NF10. Fig. 9B shows that when 5 mM of h$^+$ scavenger in the form of KI was added into the system, absence of h$^+$ resulted in a 30.4% marked reduction of removal efficiency in 60 min, denoting that photogenerated positive holes contribute to the photocatalytic oxidation of BPA to a certain extent. It is however also plausible that the introduced I$^-$ ions competed with BPA molecules in utilizing photogenerated radicals, thus leading to an overall decreased BPA degradation rate [72].

Similarly, the removal of BPA under UV photocatalytic conditions was moderately suppressed by the introduction of BQ. As observed from Fig. 9C, photocatalytic efficiency was diminished by 21.2% in the absence of $O_2{}^{\bullet-}$, which implies that $O_2{}^{\bullet-}$ participates in a moderate capacity during the oxidation process of BPA. Superoxide radicals, such as $O_2{}^{\bullet-}$ and $HO_2{}^{\bullet}$, have been reported as critical radicals during ring cleavage of aromatic compounds and the single-electron oxidation of phenols can produce phenoxyl radicals, which in the presence $O_2{}^{\bullet-}$, augments the cleavage reactions of aromatic rings [73].

$$O_2{}^{\bullet-} + h^+ \rightarrow {}^1O_2 \qquad (10)$$

As shown from Eq. (10), the singlet oxygen, $^1O_2$, is a type of reactive oxygen radical generated via the energy or electron transfer of photogenerated hole and superoxide radical. NaN$_3$, a probe reagent commonly used to scavenge $^1O_2$, exhibited marginal and negligible effect on photocatalytic removal of BPA (98.6–91.6%), even when added into the system at a high concentration (5 mM) in ensuring complete consumption of $^1O_2$. The trend from Fig. 9D shows that BPA removal rate was independent of NaN$_3$ concentration. This indicates that $^1O_2$ do not play a substantial role in the observed disappearance of BPA. The decline of 7% could be due to presence of excess NaN$_3$ molecules in the system, subsequently inhibiting BPA adsorption and UV light exposure on the catalyst. Since oxygen singlet is generated from the $O_2{}^{\bullet-}$ precursor, it can be hypothesized that scavenging of $^1O_2$ occurred only after the production of $O_2{}^{\bullet-}$ and photogenerated h$^+$. In conclusion, although $^1O_2$ was generated in the photocatalytic system, its contribution towards BPA degradation was an inconsequential one.

4. Conclusions

In summary, a novel, hierarchical nanofungus-like anatase thin film photocatalyst was successfully synthesized via a facile one-pot hydrothermal method. The superior photocatalytic performance over commercial P25-coated film presents a significant advance as Degussa P25 has been widely regarded as a benchmark photocatalyst in heterogeneous photocatalysis. The mesoporous structure and high surface area of NF10 are highly favourable for the diffusion and adsorption of BPA molecules in achieving its high photocatalytic efficiency.

From the collective crystallographic data of XRD and TEM, we can conclude that the highly crystallized NF10 product can be categorized as the body-centred tetragonal anatase phase and is polycrystalline in nature. The typical HRTEM lattice images signify that the nanocrystallites of NF10 characterized a predominant crystallographic growth along the (1 0 1) crystal plane.

The porosity and textural properties of the sample are paramount to the interaction of photocatalyst with external fluid and solid media. Based on the preceding discussions, it can be concluded that the excellent photocatalytic performance of NF10 is derived from the synergistic effects of a unique hierarchical morphology, large BET surface area, mesoporosity, high crystallinity, extended optical absorbance and increased active surface sites available.

From BPA degradation trend in the presence of interfering scavenging species, it is manifest that $^\bullet$OH was the preponderant reactive oxygen species in UV-photocatalytic oxidation processes of NF10. Photocatalytic removal of BPA was curtailed to some extent by scavengers of photogenerated h + and $O_2{}^{\bullet-}$, implying that the 2 oxygen radicals play certain extent of contributory roles, while the capacity of $^1O_2$ was trivial during photocatalytic degradation of BPA.

This one-pot hydrothermal synthesis procedure offers a facile method to synthesize highly crystallized, mesoporous anatase TiO$_2$ photocatalyst with excellent photocatalytic properties. The simple preparation strategy offers convenient scale-up for mass production in practical applications. The nanostructures fabricated in this study were directly grown on the Ti substrate thus rendering ease of catalyst separation, recycle and reuse. Despite being used for 10 continuous cycles, photocatalytic efficiency of BPA did not deteriorate more than 2%. In view of the above, we believe that this photocatalyst will be a promising candidate for engineering applications, such as photocatalytic treatment of industrial wastewaters.

Acknowledgements

Appendix A. Supplementary data

Supplementary data associated with this article can be found, in the online version, at doi:10.1016/j.apcatb.2011.09.011.

References

[1] Y.N. Xia, P.D. Yang, Y.G. Sun, Y.Y. Wu, B. Mayers, B. Gates, Y.D. Yin, F. Kim, Y.Q. Yan, Adv. Mater. 15 (2003) 353–389.
[2] X. Chen, S.S. Mao, Chem. Rev. 107 (2007) 2891–2959.
[3] Y.H. Wu, M.C. Long, W.M. Cai, S.D. Dai, C. Chen, D.Y. Wu, J. Bai, Nanotechnology 20 (2009).
[4] J. Ng, S.P. Xu, X.W. Zhang, H.Y. Yang, D.D. Sun, Adv. Funct. Mater. 20 (2010) 4287–4294.
[5] J.M. Macak, H. Tsuchiya, P. Schmuki, Angew. Chem. Int. Ed. 44 (2005) 2100–2102.
[6] J.M. Macak, M. Zlamal, J. Krysa, P. Schmuki, Small 3 (2007) 300–304.
[7] Y.M. Wang, G.J. Du, H. Liu, D. Liu, S.B. Qin, N. Wang, C.G. Hu, X.T. Tao, J. Jiao, J.Y. Wang, Z.L. Wang, Adv. Funct. Mater. 18 (2008) 1131–1137.

[8] W.Q. Fang, J.Z. Zhou, J. Liu, Z.G. Chen, C. Yang, C.H. Sun, G.R. Qian, J. Zou, S.Z. Qiao, H.G. Yang, Chem. Eur. J. 17 (2011) 1423–1427.
[9] C.X. Wang, L.W. Yin, L.Y. Zhang, Y.X. Qi, N. Lun, N.N. Liu, Langmuir 26 (2010) 12841–12848.
[10] W.K. Ho, J.C. Yu, J.G. Yu, Langmuir 21 (2005) 3486–3492.
[11] H.G. Yang, H.C. Zeng, J. Phys. Chem. B 108 (2004) 3492–3495.
[12] J. Li, H.C. Zeng, J. Am. Chem. Soc. 129 (2007) 15839–15847.
[13] J.M. Wu, T.W. Zhang, Y.W. Zeng, S. Hayakawa, K. Tsuru, A. Osaka, Langmuir 21 (2005) 6995–7002.
[14] J.M. Wu, Environ. Sci. Technol. 41 (2007) 1723–1728.
[15] X.S. Peng, A.C. Chen, Adv. Funct. Mater. 16 (2006) 1355–1362.
[16] H.G. Yang, H.C. Zeng, J. Phys. Chem. B 107 (2003) 12244–12255.
[17] J.M. Herrmann, H. Tahiri, Y. AitIchou, G. Lassaletta, A.R. GonzalezElipe, A. Fernandez, Appl. Catal. B 13 (1997) 219–228.
[18] A.C. Pierre, G.M. Pajonk, Chem. Rev. 102 (2002) 4243–4265.
[19] G.S. Wu, J.P. Wang, D.F. Thomas, A.C. Chen, Langmuir 24 (2008) 3503–3509.
[20] Y.B. Mao, M. Kanungo, T. Hemraj-Benny, S.S. Wong, J. Phys. Chem. B 110 (2006) 702–710.
[21] J.J. Wu, C.C. Yu, J. Phys. Chem. B 108 (2004) 3377–3379.
[22] J.M. Wu, H.C. Shih, W.T. Wu, Chem. Phys. Lett. 413 (2005) 490–494.
[23] M.C. Lechmann, D. Kessler, J.S. Gutmann, Langmuir 25 (2009) 10202–10208.
[24] J.Q. Huang, Z. Huang, W. Guo, M.L. Wang, Y.G. Cao, M.C. Hong, Cryst. Growth Des. 8 (2008) 2444–2446.
[25] B. Liu, H.C. Zeng, J. Am. Chem. Soc. 126 (2004) 16744–16746.
[26] J.M. Wu, B. Qi, J. Phys. Chem. C 111 (2007) 666–673.
[27] D.M. DeRosa, A.S. Zuruzi, N.C. MacDonald, Adv. Eng. Mater. 8 (2006) 77–80.
[28] P. Tengvall, H. Elwing, I. Lundstrom, J. Colloid Interface Sci. 130 (1989) 405–413.
[29] X. Hu, T. Zhang, Z. Jin, S. Huang, M. Fang, Y. Wu, L. Zhang, Cryst. Growth Des. 9 (2009) 2324–2328.
[30] S. Park, J.H. Lim, S.W. Chung, C.A. Mirkin, Science 303 (2004) 348–351.
[31] B. Liu, H.C. Zeng, J. Am. Chem. Soc. 126 (2004) 8124–8125.
[32] J.K. Yuan, K. Laubernds, Q.H. Zhang, S.L. Suib, J. Am. Chem. Soc. 125 (2003) 4966–4967.
[33] D.V. Bavykin, V.N. Parmon, A.A. Lapkin, F.C. Walsh, J. Mater. Chem. 14 (2004) 3370–3377.
[34] V.K. Lamer, R.H. Dinegar, J. Am. Chem. Soc. 72 (1950) 4847–4854.
[35] J.G. Yu, S.W. Liu, H.G. Yu, J. Catal. 249 (2007) 59–66.
[36] F. Esaka, K. Furuya, H. Shimada, M. Imamura, N. Matsubayashi, H. Sato, A. Nishijima, A. Kawana, H. Ichimura, T. Kikuchi, J. Vac. Sci. Technol. A 15 (1997) 2521–2528.
[37] K.L. Lv, X.F. Li, K.J. Deng, J. Sun, X.H. Li, M. Li, Appl. Catal. B 95 (2010) 383–392.
[38] J.H. Pan, X.W. Zhang, A.J. Du, D.D. Sun, J.O. Leckie, J. Am. Chem. Soc. 130 (2008) 11256–11257.
[39] C. Minero, G. Mariella, V. Maurino, E. Pelizzetti, Langmuir 16 (2000) 2632–2641.
[40] J.C. Yu, J.G. Yu, W.K. Ho, Z.T. Jiang, L.Z. Zhang, Chem. Mater. 14 (2002) 3808–3816.
[41] J.G. Yu, W.G. Wang, B. Cheng, B.L. Su, J. Phys. Chem. C 113 (2009) 6743–6750.
[42] H. Park, W. Choi, J. Phys. Chem. B 108 (2004) 4086–4093.
[43] J.G. Yu, H.T. Guo, S.A. Davis, S. Mann, Adv. Funct. Mater. 16 (2006) 2035–2041.
[44] C. Chen, H. Bai, C. Chang, J. Phys. Chem. C 111 (2007) 15228–15235.
[45] J. Guillot, A. Jouaiti, L. Imhoff, B. Domenichini, O. Heintz, S. Zerkout, A. Mosser, S. Bourgeois, Surf. Interface Anal. 33 (2002) 577–582.
[46] V.V. Atuchin, V.G. Kesler, N.V. Pervukhina, Z. Zhang, J. Electron Spectrosc. Relat. Phenom. 152 (2006) 18–24.
[47] N.G. Park, J. van de Lagemaat, A.J. Frank, J. Phys. Chem. B 104 (2000) 8989–8994.
[48] K. Kalyanasundaram, M. Gratzel, Coord. Chem. Rev. 177 (1998) 347–414.
[49] A. Wold, Chem. Mater. 5 (1993) 280–283.
[50] A.L. Patterson, Phys. Rev. 56 (1939) 978–982.
[51] S. Bakardjieva, J. Subrt, V. Stengl, M.J. Dianez, M.J. Sayagues, Appl. Catal. B 58 (2005) 193–202.
[52] K. Komaguchi, H. Nakano, A. Araki, Y. Harima, Chem. Phys. Lett. 428 (2006) 338–342.
[53] H.G. Yang, C.H. Sun, S.Z. Qiao, J. Zou, G. Liu, S.C. Smith, H.M. Cheng, G.Q. Lu, Nature 453 (2008) 638–641.
[54] P.P. Ewald, Acta Crystallogr. A25 (1969) 103–108.
[55] N. Serpone, D. Lawless, R. Khairutdinov, J. Phys. Chem. 99 (1995) 16646–16654.
[56] K.A. Michalow, D. Logvinovich, A. Weidenkaff, M. Amberg, G. Fortunato, A. Heel, T. Graule, M. Rekas, Catal. Today 144 (2009) 7–12.
[57] J.H. Pan, Z.Y. Cai, Y. Yu, X.S. Zhao, J. Mater. Chem. 21 (2011) 11430–11438.
[58] X. Chen, L. Liu, P.Y. Yu, S.S. Mao, Science 331 (2011) 746–750.
[59] J.Y. Chane-Ching, A. Gillorin, O. Zaberca, A. Balocchi, X. Marie, Chem. Commun. 47 (2011) 5229–5231.
[60] J.W. Ng, J.H. Pan, D.D. Sun, J. Mater. Chem. 21 (2011) 11844–11853.
[61] K.J.A. Raj, B. Viswanathan, Indian J. Chem. Sect. A 48 (2009) 1378–1382.
[62] G. Wang, Q. Wang, W. Lu, J.H. Li, J. Phys. Chem. B 110 (2006) 22029–22034.
[63] S. Agarwala, M. Kevin, A.S.W. Wong, C.K.N. Peh, V. Thavasi, G.W. Ho, ACS Appl. Mater. Interfaces 2 (2010) 1844–1850.
[64] K.S.W. Sing, D.H. Everett, R.A.W. Haul, L. Moscou, R.A. Pierotti, J. Rouquerol, T. Siemieniewska, Pure Appl. Chem. 57 (1985) 603–619.
[65] S.S. Chang, B. Clair, J. Ruelle, J. Beauchene, F. Di Renzo, F. Quignard, G.J. Zhao, H. Yamamoto, J. Gril, J. Exp. Bot. 60 (2009) 3023–3030.
[66] X.C. Wang, J.C. Yu, Y.L. Chen, L. Wu, X.Z. Fu, Environ. Sci. Technol. 40 (2006) 2369–2374.
[67] J.G. Yu, J.C. Yu, M.K.P. Leung, W.K. Ho, B. Cheng, X.J. Zhao, J.C. Zhao, J. Catal. 217 (2003) 69–78.
[68] J. Rouquerol, D. Avnir, C.W. Fairbridge, D.H. Everett, J.H. Haynes, N. Pernicone, J.D.F. Ramsay, K.S.W. Sing, K.K. Unger, Pure Appl. Chem. 66 (1994) 1739–1758.
[69] X.P. Wang, T.T. Lim, Appl. Catal. B 100 (2010) 355–364.
[70] M. Mrowetz, E. Selli, Phys. Chem. Chem. Phys. 7 (2005) 1100–1102.
[71] S.A. Walker, P.A. Christensen, K.E. Shaw, G.M. Walker, J. Electroanal. Chem. 393 (1995) 137–140.
[72] X. Wang, T.T. Lim, Appl. Catal. A 399 (2011) 233–241.
[73] P. Raja, A. Bozzi, H. Mansilla, J. Kiwi, J. Photochem. Photobiol. A: Chem. 169 (2005) 271–278.